AIAA Aviation Forum and ASCEND co-located Conference Proceedings
29 July - 2 August 2024, Las Vegas, Nevada
AIAA AVIATION FORUM AND ASCEND 2024

10.2514/6.2024-4419

2D Fluid-Body Interaction Simulation of CoFlow Jet Deflected Slipstream VTOL Transition Flight

Yan Ren [*] Gecheng Zha [†]
CoFlow Jet, LLC.
www.coflowjet.com
4649 Ponce de Leon Blvd, Suite 306, Coral Gables
FL 33146, USA
yren@coflowjet.com
gzha@coflowjet.com

Downloaded by Gecheng Zha on August 16, 2024 | http://arc.aiaa.org | DOI: 10.2514/6.2024-4419

1 Abstract

The paper presents 2D Fluid-Body Interaction (FBI) simulations of CoFlow Jet (CFJ) deflected slipstream airfoil for transition flight from hover to cruise. It includes comprehensive numerical simulations, introducing a transient scaling law to understand and predict the unsteady transition dynamics. The FBI procedure incorporates a high-fidelity structured grid CFD solver, automated mesh generation, and a 6-degree freedom body motion solver in a strongly coupled manner to accurately control and resolve the hover transition maneuver. This research demonstrates the potential to achieve a high-fidelity virtual flight testing system to improve hover transition reliability, safety, efficiency, safety, and noise reduction, which are crucial for advanced air mobility (AAM) technology development.

2 Introduction

Electric vertical takeoff/landing (eVTOL) [1] fixed wing aircraft play a critical role in the current transformation of urban transportation and eCommerce goods shipping. However, it must overcome public acceptance barriers to prevail, including: 1) safety [2–5]; 2) noise; 3) affordability. The safety and affordability could be achieved by reducing system complexity to have high reliability and low manufacturing cost. High transportation productivity $[R(range) \times W(gross\ weight)/$per unit energy consumed] will contribute to affordability with reduced operating cost. High productivity also mitigates noise due to reduced specific weight [W/(R× payload)] and thus disk loading. Aircraft productivity efficiency is determined by C_L^2/C_D [6].

The current Advanced Air Mobility (AAM) movement of eVTOL with fixed wing aircraft has made enormous progress represented by Joby's successful flights with low noise. Compared with rotorcraft, the fixed wing eVTOL configurations with distributed propulsors have lower noise, higher efficiency, and faster cruise speed. However, the current eVTOL hover technology is still based on the conventional rotorcraft principles with propellers facing upward, which requires tiltrotors, tiltwings, or lift-plus-cruise configurations for transition

An aircraft component used for the entire flight envelope is most efficient to reduce weight and drag. A component only used partially in a flight envelope is an "inefficient weight". For the state-of-the-art (SoA) fixed wing eVTOL, the inefficient weights include: 1) the hover lift propellers of a lift plus configuration, which are only used at hover, not at cruise. 2) the wings of all the SoA VTOL aircraft

---

[*] CoFlow Jet, LLC., CTO, Ph.D., AIAA member
[†] CoFlow Jet, LLC., President, AIAA Associate Fellow, Professor of the University of Miami

Copyright © 2024 by All authors of the manuscript. . Published by the American Institute of Aeronautics and Astronautics, Inc., with permission.

Downloaded by Gecheng Zha on August 16, 2024 | http://arc.aiaa.org | DOI: 10.2514/6.2024-4419

because they are only used at cruise not at hover, and 3) vertical and horizontal tails as they are only used in the occasion of disturbance.

In addition to the efficiency factors mentioned above that determines the vehicle's payload and range, a critical flight maneuver of eVTOL is the transition from hover takeoff to cruise and from cruise to hover landing. The challenge for transition is that the sufficient lift must be established before the high cruise speed is reached (takeoff) or after the cruise speed is aborted (landing).

The deflected slipstream enabled by coflow jet to be described below provides a new technology option that has the potential to significantly improve the cruise efficiency and hover transition performance.

2.1 Deflected Slipstream VTOL

The deflected slipstream (DS) concept pioneered by Kuhn and Draper in the late 1950's [7–9] generates hover lift by deflecting the slipstream from the propeller downward using a deflected flap. Once airborne, the flap is retracted for high-speed cruise. A 90° deflected slipstream would turn a full horizontal propeller thrust to a vertical lift. However, flow suffers severe separation when the flap angle is large. A double-plain flap system tested was able to deflect the flow by 45° [7]. A double-slotted flap [8] increased the deflection to 63°. Such a flow deflection is not sufficient for hover, in particular with the ground effect. The efforts using DS for VTOL were abandoned in 1960's. Antcliff et al at NASA [1] recently revisited the DS concept and suggested using CoFlow Jet (CFJ) flow control to enhance the flow turning. They envision that the deflected slipstream eVTOL as the second generation UAM vehicles "could provide benefits in cruise efficiency, weight, noise, reliability, and maintainability, and offer safer transition characteristics" [1].

2.2 Deflected Slipstream Enabled by CoFlow Jet

CFJ is a zero-net-mass-flux (ZNMF) active flow control technique recently developed by Zha and his team [6, 10–17, 17–21]. As illustrated in Fig. 1, a small amount of mass flow is drawn into the airfoil near the trailing edge, pressurized and energized by a micro-compressor system inside the airfoil, and then injected near the leading edge in the direction tangent to the main flow. CFJ achieves ultra-high lift coefficient exceeding the theoretical limit [6], thrust generation, and very high stall angle of attack (e.g., 70°) with low energy expenditure.

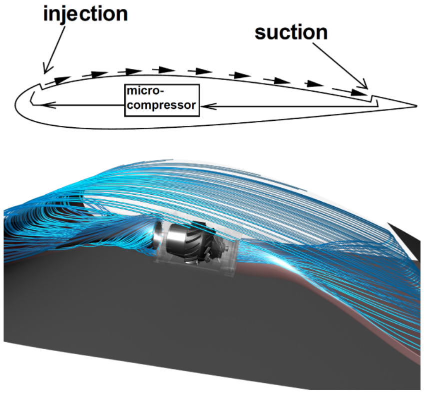

Figure 1: CFJ airfoil concept and micro-compressor embedded.

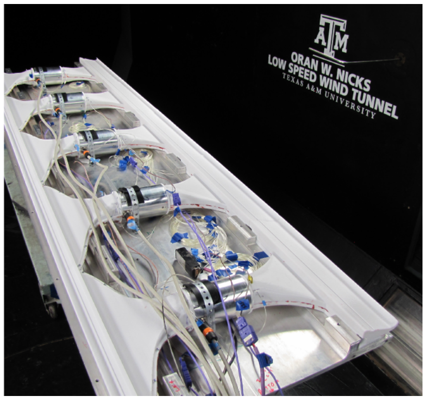

Figure 2: Photo of the wind tunnel tested airfoil with 5 compressors embedded.

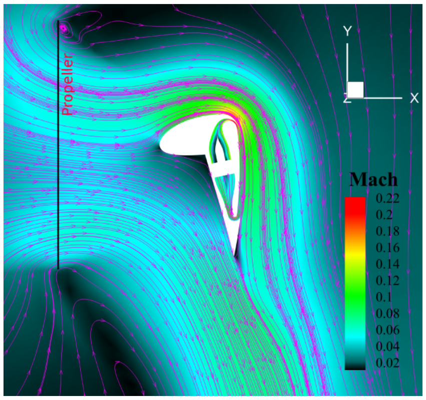

Figure 3: 3D CFD simulated DS-CFJ airfoil at static hover conditions.

Fig. 2 is the photo of the CFJ-NACA6421 airfoil recently tested in a wind tunnel with 5 compressors embedded inside the airfoil along the span [22]. A C_{Lmax} of 8.6 is achieved, far greater than 1.5 of the baseline airfoil [22]. The CFJ airfoil also generates very high thrust up to $C_D = -1.0$. The

Downloaded by Gecheng Zha on August 16, 2024 | http://arc.aiaa.org | DOI: 10.2514/6.2024-4419

operating range of CFJ airfoil without stall is dramatically increased. The CFJ airfoil has very low energy expenditure, which is the unique feature enabling CFJ wing to obtain very high productivity efficiency at cruise when the flow is benign at low angle of attack [19, 23–25].

Fig. 3 is the mid-section of CFD result for the 3D DS-CFJ wing with the micro-compressor (Fig. 1) embedded in the single plain flap. It shows that the slipstream from the propeller is deflected 88° by the CFJ flap at static hover condition. Single plain flaps will have the lowest mechanical complexity basically the same as conventional takeoff/landing (CTOL) aircraft, much lower than the titling wings or articulating propellers. The ground effect can be eliminated if the wing is 2.3D above the ground (D: prop. diameter) or the propeller is slightly mounted upward as shown in Fig. 4 with the wing 1.5D above the ground. The slipstream is turned 90°, hits the ground and bifurcates to flow upstream and downstream. Fig. 5 shows the 2D cruise flow of the DS-CFJ airfoil with the flap retracted at Mach 0.15. It has C_L=1.4, C_L/C_D=107.8, $C_L/(C_D + P_c)$ =74 (P_c: CFJ power coefficient), and C_μ=0.03. CFJ appears to be the only active flow control that could achieve extraordinary cruise efficiency due to its low energy expenditure [17, 19, 23, 26, 27]. Conventional airfoil with C_L=1.4 would be nearly stalled with a large drag and poor C_L/C_D.

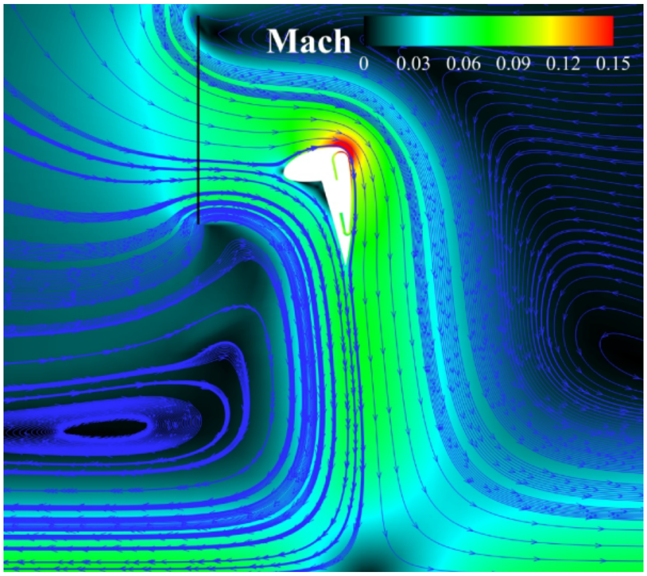

Figure 4: Hover with ground effect.

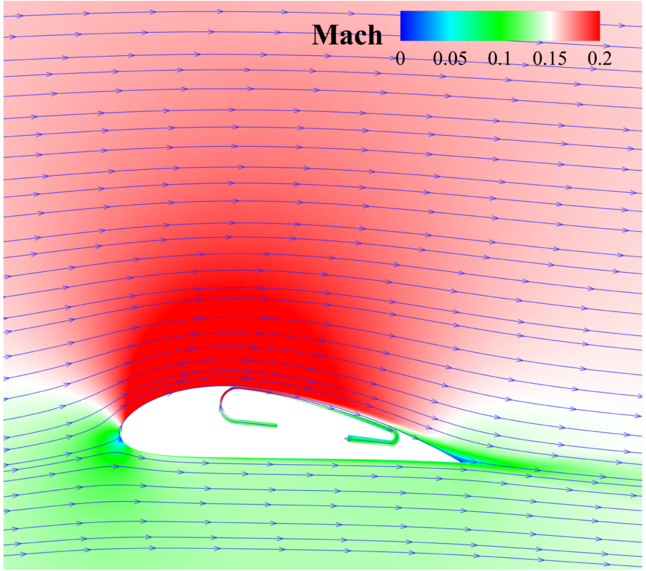

Figure 5: DS-CFJ airfoil at high efficiency cruise.

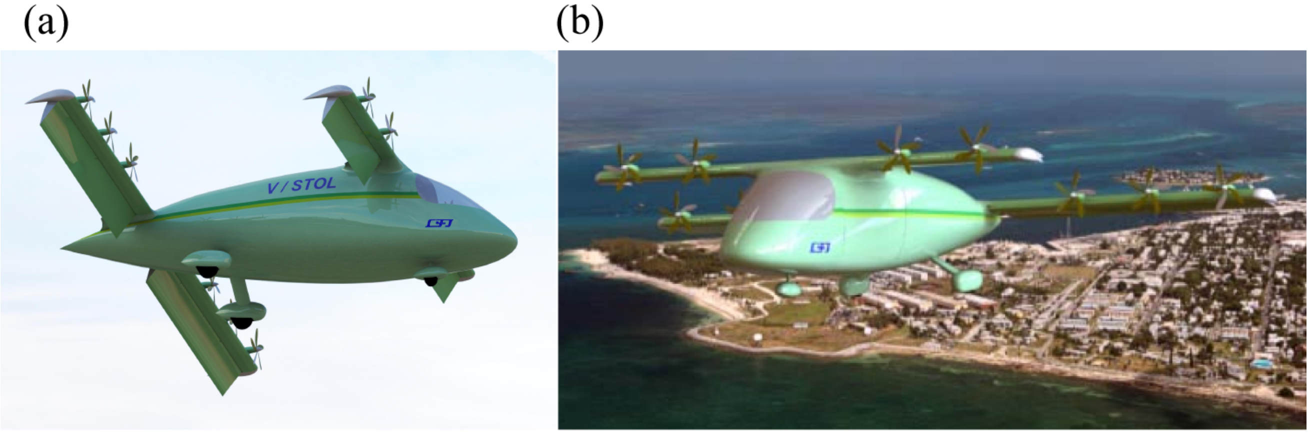

Figure 6: (a) DS-eVTOL at hover with the plain CFJ flap down and (b) cruise with the flap retracted.

Downloaded by Gecheng Zha on August 16, 2024 | http://arc.aiaa.org | DOI: 10.2514/6.2024-4419

2.3 Novel eVTOL Concept Enabled by Deflected Slipstream with CoFlow Jet

The novel deflected slipstream CFJ eVTOL (DS-CFJ eVTOL) concept under development in our company illustrated in Fig. 6 has a tandem wing configuration with single plain flaps deflected down for hover and retracted for cruise. A tandem wing configuration provides high hover stability with two lifting vectors [28]. The distributed propellers and micro-compressors embedded inside the wings will be powered by electric batteries individually to ensure high redundancy and safety. This vehicle will resemble CTOL with substantially less complexity than the SoA eVTOL using tilting wings, or articulating propellers, or lift plus configurations. Our preliminary design and analysis based on 3D CFD simulation indicates that DS-CFJ eVTOL can achieve very high cruise C_L and C_L/C_{D_c}. However, no study is done to investigate the transition between hover and cruise.

The objective of this paper is to develop a model and procedure for numerical simulation of DS-CFJ hover transition, which can simulate the full fluid-body interaction determined by the system motion dynamics. As the first step, this paper is to develop a model for 2D simulation of the transition.

3 Transition from hover to cruise

The purpose of this paper is to numerically simulate the 2D unsteady transition process, as shown in Fig. 7, between takeoff and cruise for the DS-CFJ eVTOL system. The following transient scaling law for the DS-CFJ airfoil will be developed:

$$L,\ D,\ M = f(\beta(t), V(t), C_\mu(t), \Delta P(t), t) \tag{1}$$

where $\beta(t)$ is the flap deflection angle, $C_\mu(t)$ is the injection momentum coefficient, and $\Delta P(t)$ is the propeller strength.

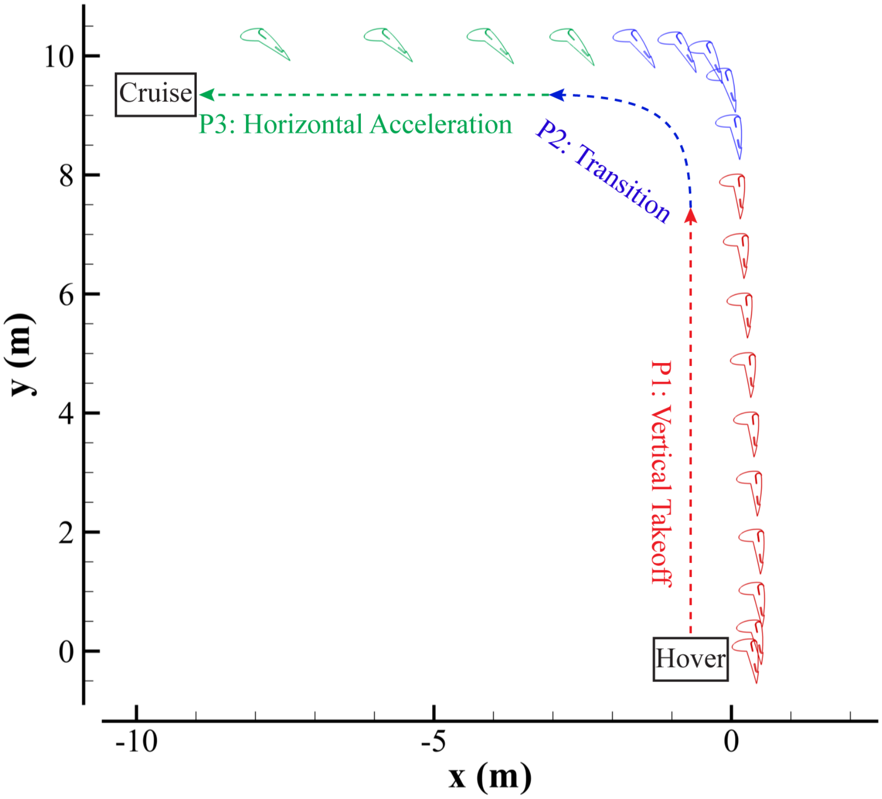

Figure 7: Simulated flight trajectory of the DS-CFJ airfoil in transitional flight from hover to cruise, illustrating the three phases: P1 - Vertical Takeoff, P2 - Transition, and P3 - Horizontal Acceleration.

Downloaded by Gecheng Zha on August 16, 2024 | http://arc.aiaa.org | DOI: 10.2514/6.2024-4419

The simulated flight trajectory for the DS-CFJ airfoil in transitional flight from hover to cruise is depicted in Fig. 7. The trajectory encompasses three distinct phases: vertical takeoff (P1), transition (P2), and horizontal acceleration (P3). In Phase I, the airfoil initiates from a hover position and ascends vertically, achieving the desired altitude. During Phase II, the transition phase, the airfoil maneuvers from a vertical climb to a horizontal flight path. This phase involves a gradual reduction in vertical velocity and the initiation of horizontal acceleration. Phase III represents the horizontal acceleration phase, where the airfoil continues to accelerate horizontally to reach the desired cruise speed. Throughout these phases, the control strategies effectively manage the flap angle (β), propeller strength (ΔP), and micro-compressor momentum coefficient (C_μ) to maintain stability and achieve the desired flight trajectory.

4 Methodology

4.1 DS-CFJ airfoil modeling and performance evaluation

The DS-CFJ airfoil modeling focuses on a 21% thickness DS-CFJ-NACA 6421 airfoil, which has been optimized in previous studies for improved aerodynamic performance. This airfoil features a substantial Co-Flow Jet (CFJ) flap with a length constituting 66% of the chord length, providing significant control and lift enhancement capabilities. The chord length c of the airfoil is 1 m. The front portion of the airfoil is designed to operate at an angle of attack (AoA) α of 5 degrees, which is also the optimized angle of attack for cruising conditions. Additionally, a propeller with a diameter D of 1.321 m is installed in front of the airfoil. The configuration details, including the flap angle β and the exact location of the propeller, can be seen in Fig. 8. This configuration aims to leverage the synergetic effects of the CFJ flap and the propeller to achieve enhanced aerodynamic efficiency and performance.

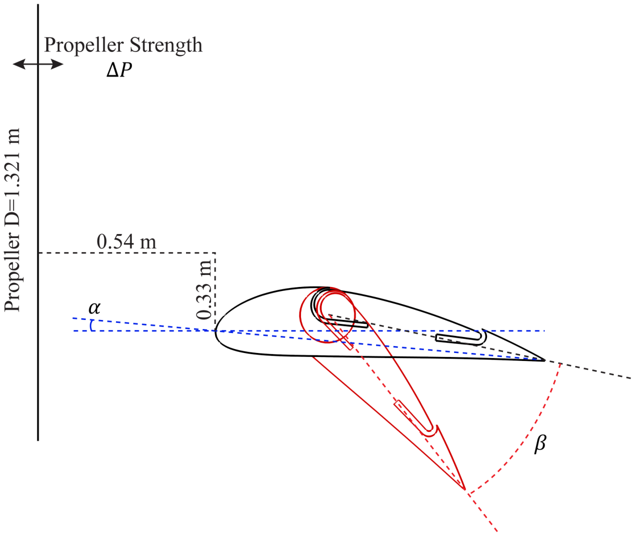

Figure 8: DS-CFJ NACA 6421 Airfoil.

The momentum and pressure at the injection and suction slots produce a reactionary force, which is automatically measured by the force balance in wind tunnel testing. However, for CFD simulation, the full reactionary force needs to be included. Using control volume analysis, the reactionary force can be calculated using the flow parameters at the injection and suction slot opening surfaces. Zha et al. [10] give the following formulations to calculate the lift and drag due to the jet reactionary force for a CFJ airfoil. By considering the effects of injection and suction jets on the CFJ airfoil, the expressions for these reactionary forces are given as :

$$F_{x_{cfj}} = (\dot{m}_j V_{j1} + p_{j1} A_{j1}) * cos(\theta_1 - \alpha) - (\dot{m}_j V_{j2} + p_{j2} A_{j2}) * cos(\theta_2 + \alpha) \tag{2}$$

$$F_{y_{cfj}} = (\dot{m}_{j1} V_{j1} + p_{j1} A_{j1}) * sin(\theta_1 - \alpha) + (\dot{m}_{j2} V_{j2} + p_{j2} A_{j2}) * sin(\theta_2 + \alpha) \tag{3}$$

where the subscripts 1 and 2 stand for the injection and suction respectively, and θ_1 and θ_2 are the angles between the injection and suction slot's surface and a line normal to the airfoil chord. α is the angle of attack.

The total lift and drag on the airfoil can then be expressed as:

$$D = R'_x - F_{x_{cfj}} \tag{4}$$

$$L = R'_y - F_{y_{cfj}} \tag{5}$$

where R'_x and R'_y are the surface integral of pressure and shear stress in x (drag) and y (lift) direction excluding the internal ducts of injection and suction. For CFJ wing simulations, the total lift and drag are calculated by integrating Eqs.(4) and (5) in the spanwise direction.

The jet momentum coefficient C_μ is a parameter used to quantify the jet intensity. It is defined as:

$$C_\mu = \frac{\dot{m} V_j}{\frac{1}{2} \rho_\infty {V_\infty}^2 S} \tag{6}$$

where $\dot{m}$ is the injection mass flow, V_j is the mass-averaged injection velocity, ρ_∞ and V_∞ denote the free stream density and velocity, and S is the planform area. In this study, the CFJ injection momentum coefficient is controlled by the compressor RPM that also determines the compressor power.

4.2 Flow solver with implicit coupling fluid and body interaction

The CFD solver of the DS-CFJ airfoil is conducted using our in-house high order CFD code, FASIP (Flow-Acoustics-Structure Interaction Package) developed under various government agencies(AFOSR, NASA, ARO, NSF, GUIde) [14, 17, 19, 20, 29–52]. FASIP has high order WENO schemes (5th and 7th) [30–38, 53] for the inviscid fluxes and fully conservative 4th and 6th order central differencing schemes for the viscous fluxes [30, 31]. It incorporates advanced turbulence modeling with RANS, IDDES, and LES. The CFD simulation and FASIP code are intensively validated with CFJ experiment for aerodynamic forces and power consumption [6, 14, 17, 21, 39, 40, 49, 50, 52].

In order to simulate the unsteady transition process, an implicit coupling fluid and body interaction method is developed and embedded in our FASIP flow solver. In general, equations of motion of a rigid body with 6 degrees of freedom can be written as:

$$\vec{F}(t) = m \frac{d\vec{V}_G}{dt}, \quad \vec{\tau}_c(t) = I \cdot \frac{d\vec{\Omega}}{dt} + \vec{\Omega} \times (I \cdot \vec{\Omega}) \tag{7}$$

where $\vec{F}(t)$ is the total force, including the net body force $\vec{F}_G$ contributed from gravity, aerodynamic force $\vec{F}_A$ on surface, other external forces $\vec{F}_E$. $\vec{\tau}_c(t)$ is the total torque with respect to the mass center of body, which includes $\vec{\tau}_A$ generated by aerodynamic force, and torque $\vec{\tau}_E$ induced by other external forces. $\vec{V}_G$ is velocity at mass center, m is body mass and I is the moment of inertia tensor about mass

Downloaded by Gecheng Zha on August 16, 2024 | http://arc.aiaa.org | DOI: 10.2514/6.2024-4419

Downloaded by Gecheng Zha on August 16, 2024 | http://arc.aiaa.org | DOI: 10.2514/6.2024-4419

center. $\vec{\Omega}$ is the angular velocity vector. The aerodynamic force $\vec{F}_A$ and torque $\vec{\tau}_A$ are obtained by the surface integration of pressure p and viscous stress tensor σ, and can be given as:

$$\vec{F}_A = \int_s (\sigma \cdot \vec{n} - p\vec{n})ds, \quad \vec{\tau}_A = \int_s (\sigma \cdot \vec{n} - p\vec{n}) \times \vec{r}ds \tag{8}$$

where $\vec{n}$ is the outer normal to the body surface, and $\vec{r}$ is the vector from mass center to certain surface element.

Coupling between fluid and body can be roughly categorized as explicit (loosely) and implicit (strongly) methods. In the explicit method, the left hand side force and torque in discretized form of Eqns. (3) and (4) are replaced by $\vec{F}^n$ and $\vec{\tau}^n$ respectively, which are obtained from the previous time step. However, the explicit method subjects to conditionally stable, since the n+1 time step translational and angular velocities are being calculated from the forces at n-time step. In the implicit method, $\vec{F}^{n+1}$ and $\vec{\tau}_c^{n+1}$ are substituted into the discretized equation of body motion, therefore both sides are at n+1 time step, and can be expressed as:

$$\vec{F}^{n+1} = m\frac{\vec{V}_G^{n+1} - \vec{V}_G^n}{\Delta t}, \quad \vec{\tau}_c^{n+1} = I \cdot \frac{\vec{\Omega}^{n+1} - \vec{\Omega}^n}{\Delta t} + \vec{\Omega}^n \times (I \cdot \vec{\Omega}^n) \tag{9}$$

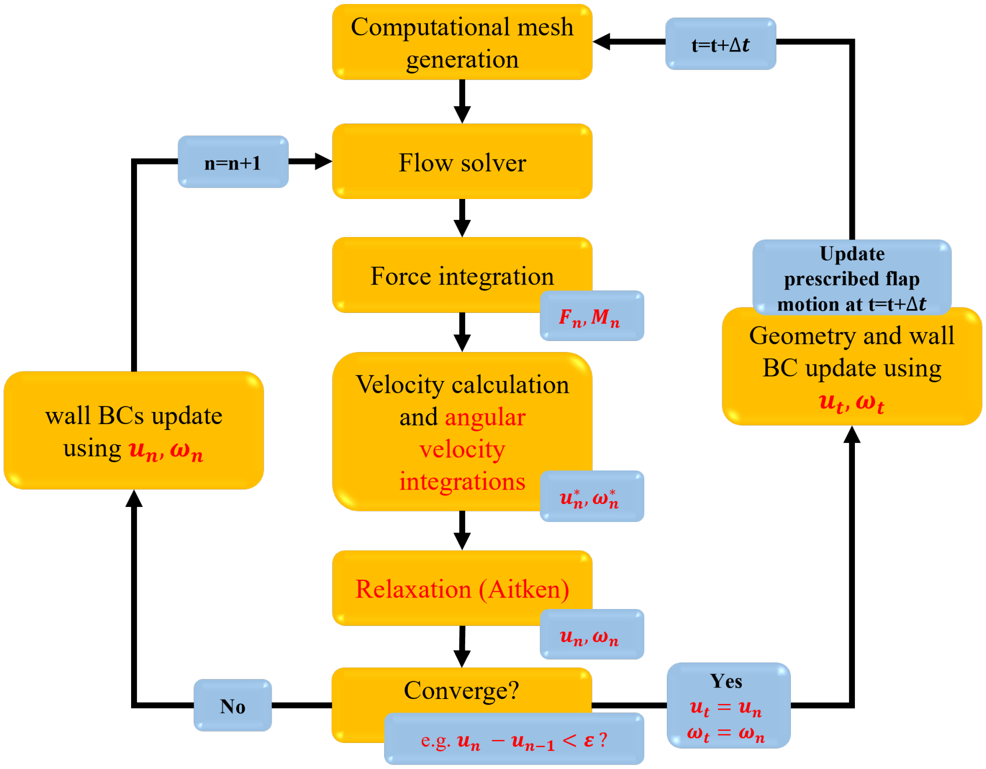

Figure 9: Flow chart of the implicit coupling fluid and body interaction (FBI) process.

The implicit algorithm we have applied to fluid and body coupling is summarized in the flow chart of Fig. 9. At each time step, first generate the computational mesh and set the initial time $t = t_0$, then solve the flow equations using the current mesh and boundary conditions. Integrate the forces (F_n) and moments (M_n) on the body surface. Calculate the linear and angular velocities (u_n^* and ω_n^*) based on the integrated forces and moments. Apply relaxation techniques (Aitken) to update the velocities (u_n and ω_n). Check for convergence by comparing the current velocities with the previous iteration

Downloaded by Gecheng Zha on August 16, 2024 | http://arc.aiaa.org | DOI: 10.2514/6.2024-4419

$(u_n - u_{n-1} < \epsilon)$. If convergence is not achieved, set $n = n + 1$ (n is the inner iteration index within a physical time step) and update the wall boundary conditions using the current velocities and repeat from the flow solver step. If convergence is achieved, update the prescribed flap motion at $t = t + \Delta t$, and update the geometry and wall boundary conditions using the current velocities (u_t and ω_t). Return to the flow solver step and repeat the process for the next physical time step. Iterate the process of solving fluid dynamics using the updated body velocities as boundary conditions and of solving body dynamics, until the convergence criteria of pressure and body velocities are obtained.

The automated mesh generation process, essential for implementing the FBI, is illustrated in Fig. 10. The plots show the mesh around the airfoil for different flap angles, illustrating the capability of the mesh generation algorithm to handle complex geometries and flow conditions. In the current two-dimensional (2D) study, the translational degrees of freedom (DOFs) in the x and y directions are permitted. All other DOFs are constrained due to the nature of the 2D airfoil simulation. Given the absence of a fuselage and other three-dimensional (3D) structures, rotational DOFs are not applicable.

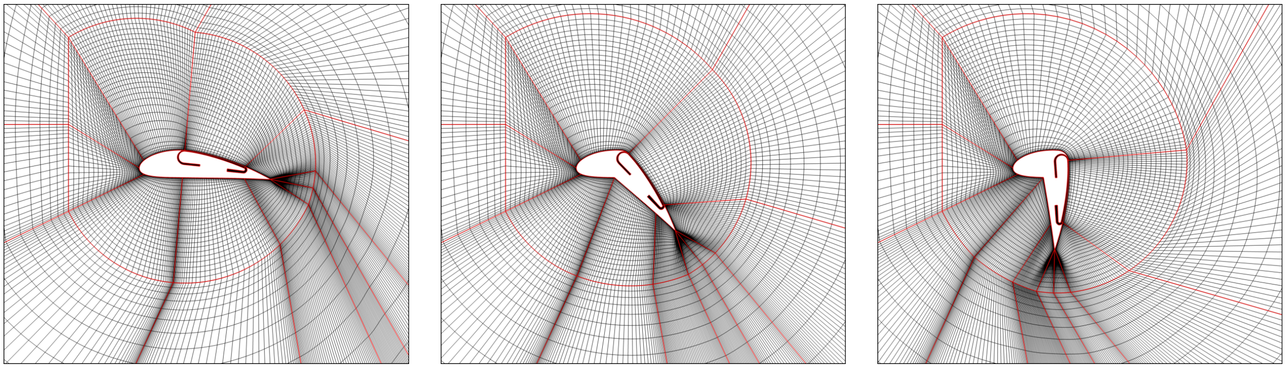

(a) (b) (c)

Figure 10: Automatic mesh generation around the airfoil for different flap angles: (a) $\beta = 0°$, (b) $\beta = 40°$, (c) $\beta = 80°$.

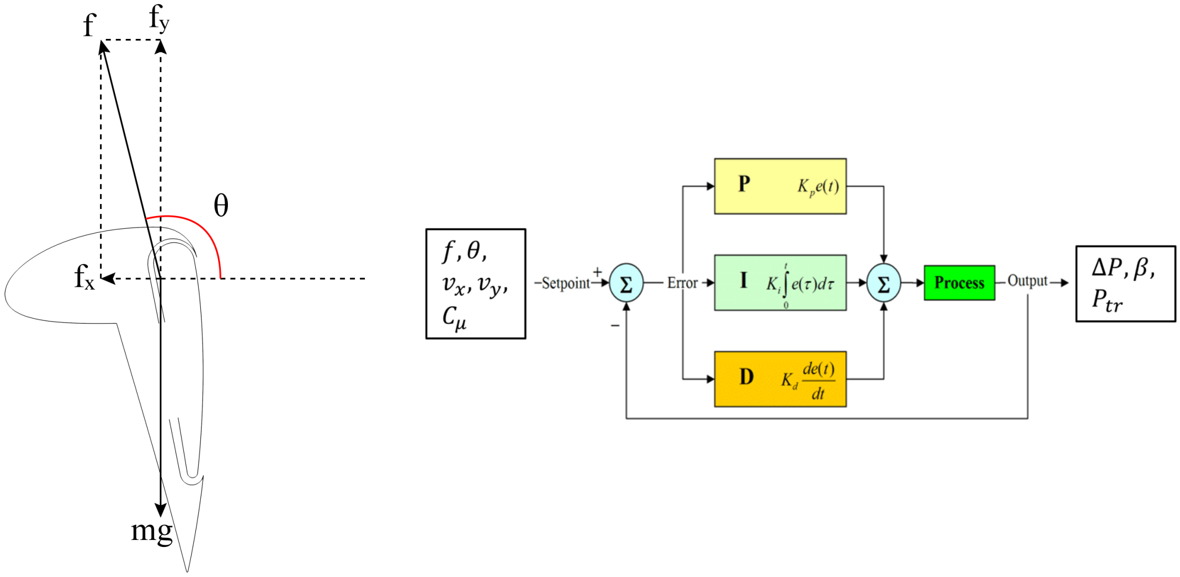

(a) (b)

Figure 11: (a) Resultant force amplitude f and force angle θ as control parameters. (b) PID control system for managing flight parameters.

4.3 Automatic control during transitional flight

Automatic control plays a critical role during the transitional flight process from hover to cruise. In the current 2D transitional flight study, several parameters are monitored and controlled: (1) the amplitude of the resultant force f and the force angle θ (Fig. 11(a)); (2) vertical and horizontal speeds; (3) the jet momentum coefficient C_μ. PID controllers are employed as depicted in Fig. 11(b). The aforementioned parameters serve as system outputs, which also act as inputs to the PID controllers. The outputs of the PID controllers (system inputs) include: (1) propeller strength ΔP (Fig. 8); (2) DS-CFJ airfoil flap angle β (Fig. 8); (3) the micro-compressor total pressure ratio (Fig. 1). Detailed control strategies for different phases of the transitional flight will be elaborated in the results section.

5 Results

A two-dimensional (2D) DS-CFJ airfoil fluid-body interaction simulation is conducted. The airfoil dynamic motion is evaluated based on the specifications of an assumed e-plane, as listed in Tab. 1. As described in Fig. 7, the entire transitional flight consists of three distinct phases: Phase I - vertical takeoff, Phase II - transition, and Phase III - horizontal acceleration. To maintain flow attachment and prevent stall across all phases, the micro-compressor jet momentum coefficient is set to $C_\mu = 0.8$, and is held as constant in this simulation to simplify the control process. This coefficient is computed using a far-field reference velocity of $V_\infty = 13.6\,\text{m/s}$ (Eqn. 6).

Table 1: E-plane specifications

Mass	1500 kg
Wing Span	20 m
Wing Chord	1 m
Horizontal Acceleration Limit	0.25 g
Vertical Acceleration Limit	0.25 g
Vertical Takeoff Speed	2.7 m/s

5.1 Phase I: Vertical takeoff

Phase I consists of two parts: (1) vertical acceleration and (2) vertical takeoff at constant speed. For part 1, the flap angle β is used to control the resultant force angle θ, while the propeller strength ΔP is used to control the resultant force amplitude f. Fig. 12 shows the Mach contours of the flow around the DS-CFJ airfoil during part 1, from $t = 0.184\,\text{s}$ to $t = 1.654\,\text{s}$. It is observed that the flow remains attached to the airfoil, allowing the airfoil to accelerate from rest to $2.7\,\text{m/s}$.

In part 2, the control of θ is maintained via the flap angle β, similar to part 1. However, part 2 also involves speed control to maintain a constant vertical speed of $2.7\,\text{m/s}$. Fig. 13 illustrates the Mach contours of the flow around the airfoil during part 2, from $t = 2.022\,\text{s}$ to $t = 3.493\,\text{s}$. The Mach contours indicate that the flow remains attached to the airfoil, ensuring stable vertical takeoff at the constant speed.

Downloaded by Gecheng Zha on August 16, 2024 | http://arc.aiaa.org | DOI: 10.2514/6.2024-4419

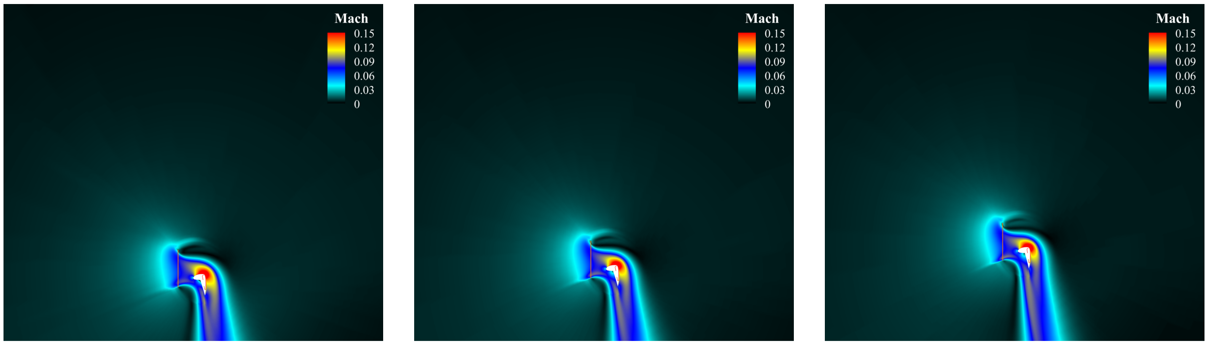

(a) $t = 0.184\,\mathrm{s}$ (b) $t = 0.551\,\mathrm{s}$ (c) $t = 0.919\,\mathrm{s}$

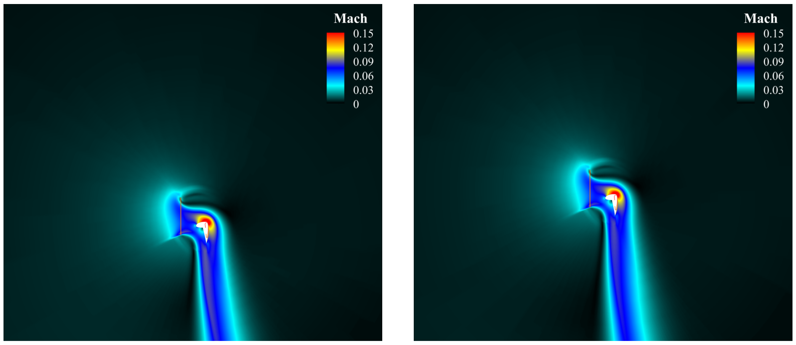

(d) $t = 1.287\,\mathrm{s}$ (e) $t = 1.654\,\mathrm{s}$

Figure 12: Mach contours around the DS-CFJ airfoil during Phase I, part 1 (vertical acceleration) from $t = 0.184\,\mathrm{s}$ to $t = 1.654\,\mathrm{s}$: (a) $t = 0.184\,\mathrm{s}$, (b) $t = 0.551\,\mathrm{s}$, (c) $t = 0.919\,\mathrm{s}$, (d) $t = 1.287\,\mathrm{s}$, (e) $t = 1.654\,\mathrm{s}$.

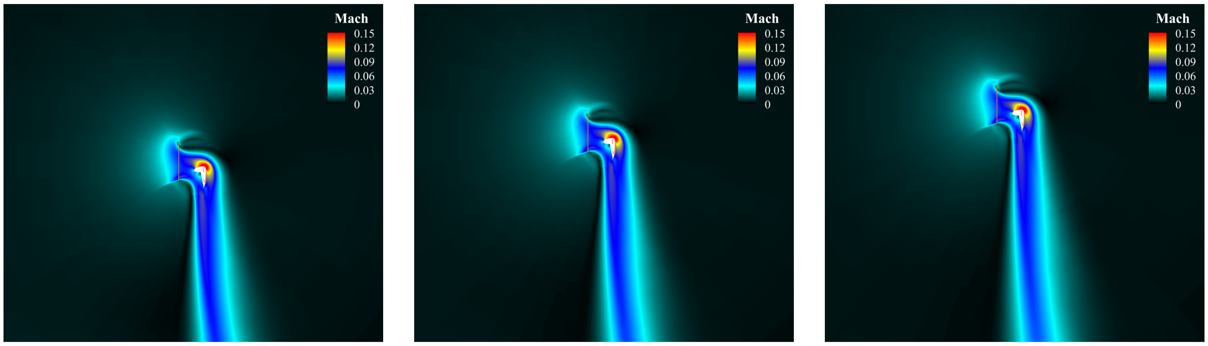

(a) $t = 2.022\,\mathrm{s}$ (b) $t = 2.390\,\mathrm{s}$ (c) $t = 2.757\,\mathrm{s}$

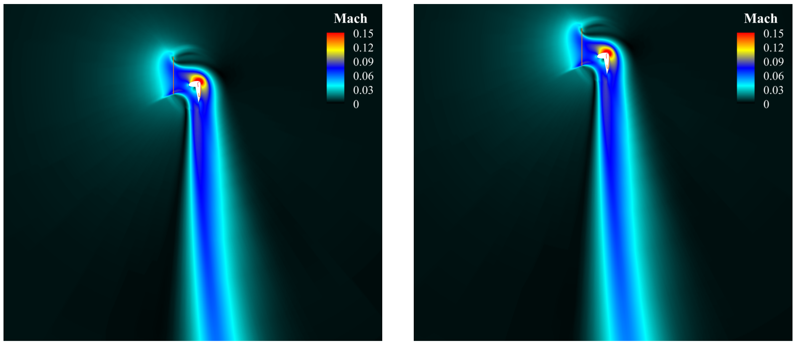

(d) $t = 3.125\,\mathrm{s}$ (e) $t = 3.493\,\mathrm{s}$

Figure 13: Mach contours around the DS-CFJ airfoil during Phase I, part 2 (vertical takeoff at constant speed) from $t = 2.022\,\mathrm{s}$ to $t = 3.493\,\mathrm{s}$: (a) $t = 2.022\,\mathrm{s}$, (b) $t = 2.390\,\mathrm{s}$, (c) $t = 2.757\,\mathrm{s}$, (d) $t = 3.125\,\mathrm{s}$, (e) $t = 3.493\,\mathrm{s}$.

Downloaded by Gecheng Zha on August 16, 2024 | http://arc.aiaa.org | DOI: 10.2514/6.2024-4419

Downloaded by Gecheng Zha on August 16, 2024 | http://arc.aiaa.org | DOI: 10.2514/6.2024-4419

Fig. 14 presents the time history of key flight parameters during Phase I of the 2D DS-CFJ airfoil fluid-body interaction simulation, focusing on propeller strength, beta angle, vertical acceleration, theta angle, and vertical speed. During part 1 of Phase I, the vertical acceleration limit is set to 0.25 g, and the theta angle is controlled to 90°. Fig. 14(a) depicts the propeller strength (ΔP) over time, showing the initial high power for acceleration and the subsequent stabilization. Fig. 14(b) illustrates the beta angle (β), which regulates the resultant force angle, varying initially but stabilizing around 75°. Fig. 14(c) shows the vertical acceleration (a_y), depicting an initial acceleration phase that stabilizes around 0.25 g after approximately 1.5 seconds. Subsequently, the airfoil exhibits zero acceleration, maintaining a constant vertical speed. Fig. 14(d) shows the theta angle (θ), which is controlled to maintain the resultant force angle at 90°, stabilizing after some initial oscillations. Finally, Fig. 14(e) displays the vertical speed (v), indicating the airfoil's acceleration from rest to a stable vertical speed of 2.7 m/s within the first 1.5 seconds. This constant speed is then maintained during part 2 of Phase I. These plots collectively demonstrate the effectiveness of the control strategies employed during Phase I to achieve a stable vertical takeoff.

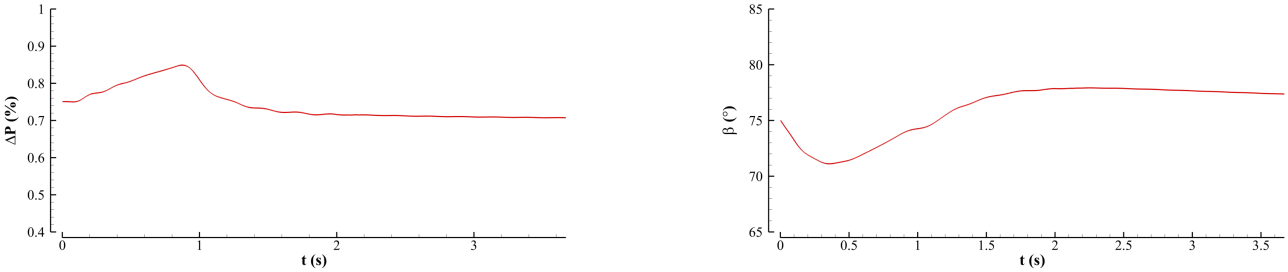

(a) Propeller strength (ΔP) (b) Flap angle (β)

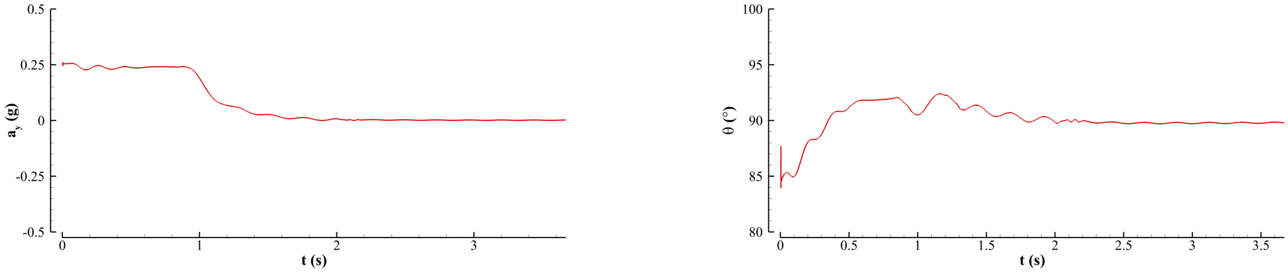

(c) Vertical acceleration (a_y) (d) Force vector angle (θ)

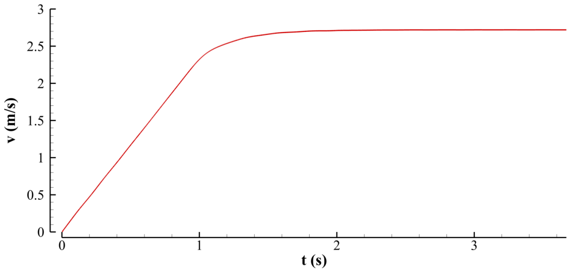

(e) Vertical speed (v)

Figure 14: Time history of key flight parameters during Phase I: (a) Propeller strength (ΔP), (b) Flap angle (β), (c) Vertical acceleration (a_y), (d) Force vector angle (θ), and (e) Vertical speed (v).

5.2 Phase II: Transition

Phase II represents the transition phase, during which the vertical velocity decreases to zero and remains at zero thereafter. Concurrently, the airfoil accelerates horizontally, with the horizontal acceleration increasing from zero to 0.25 g. Under these conditions, the force vector angle θ is calculated to be 104.036°. The control strategy for this phase involves setting the vertical speed setpoint to zero and the θ setpoint to 104.036°, with the flap angle β and the propeller strength ΔP used to achieve these targets. Fig. 15 presents the Mach contours of the flow around the DS-CFJ airfoil during Phase II, spanning from $t = 3.860\,\mathrm{s}$ to $t = 5.331\,\mathrm{s}$. It is observed that the flow remains attached to the airfoil despite significant changes in the flap angle during this phase. This demonstrates the robustness of the control strategy in maintaining flow attachment and achieving the desired transition.

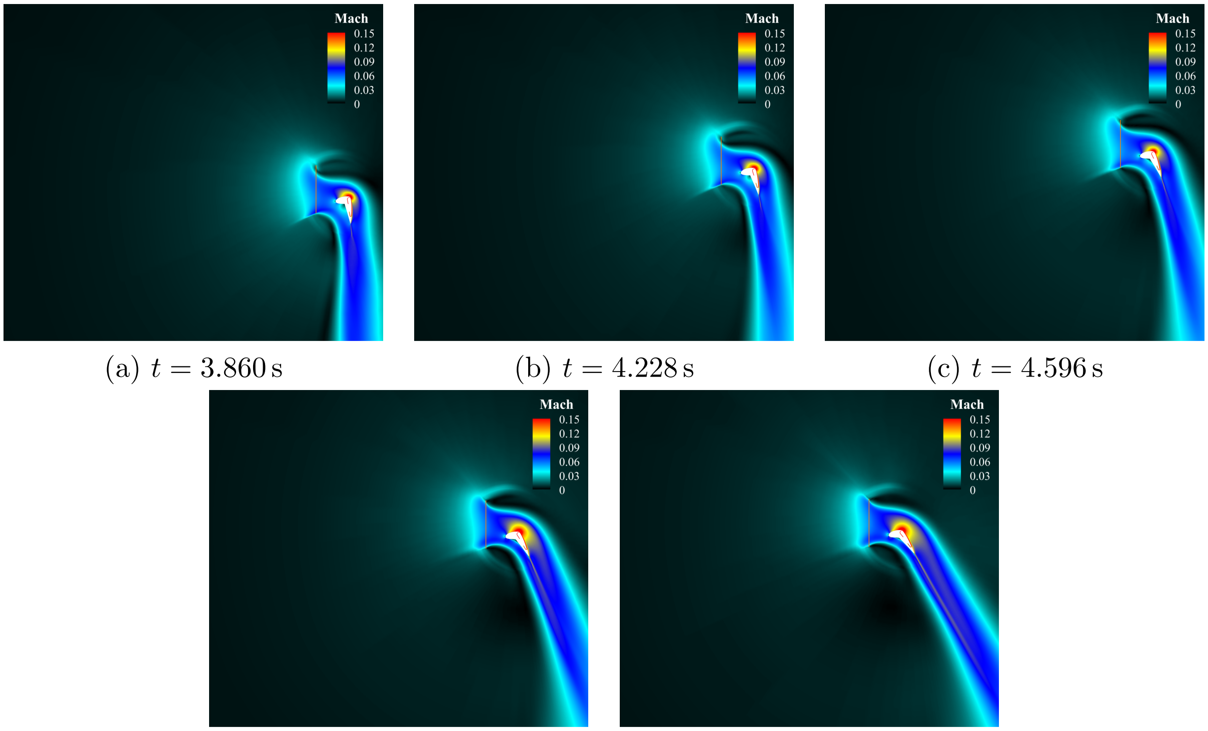

(a) $t = 3.860\,\mathrm{s}$ (b) $t = 4.228\,\mathrm{s}$ (c) $t = 4.596\,\mathrm{s}$

(d) $t = 4.963\,\mathrm{s}$ (e) $t = 5.331\,\mathrm{s}$

Figure 15: Mach contours around the DS-CFJ airfoil during Phase II (transition phase) from $t = 3.860\,\mathrm{s}$ to $t = 5.331\,\mathrm{s}$.

Fig. 16(a) presents the time history of propeller strength (ΔP), revealing initial fluctuations followed by stabilization. Fig. 16(b) depicts the beta angle (β), which is adjusted to manage the resultant force angle, initially varying but eventually stabilizing as the transition phase progresses. The horizontal acceleration (a_x), shown in Fig. 16(c), demonstrates the increase from zero to 0.25 g. Fig. 16(d) illustrates the theta angle (θ), controlled to maintain the resultant force angle at 104.036°, with stabilization occurring after initial oscillations. Finally, Fig. 16(e) displays the vertical speed (v), highlighting the reduction to zero, which is then maintained throughout Phase II. These plots collectively highlight the effectiveness of the control strategies implemented to achieve a stable transition during Phase II, differentiating it from the vertical takeoff phase by focusing on horizontal acceleration and maintaining zero vertical speed.

Downloaded by Gecheng Zha on August 16, 2024 | http://arc.aiaa.org | DOI: 10.2514/6.2024-4419

Downloaded by Gecheng Zha on August 16, 2024 | http://arc.aiaa.org | DOI: 10.2514/6.2024-4419

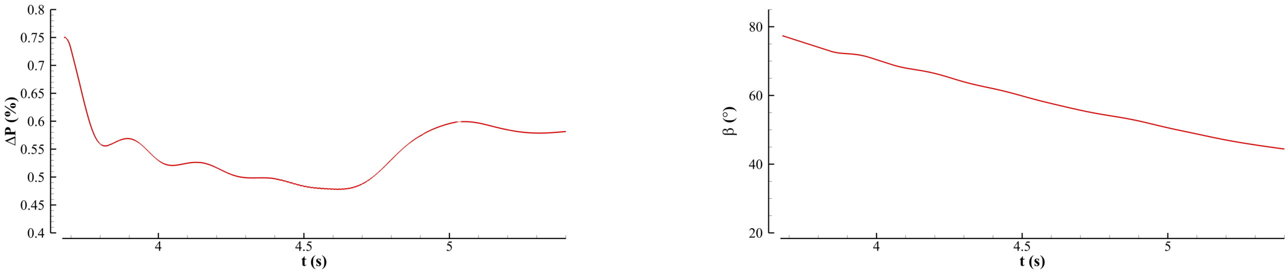

(a) Propeller strength (ΔP)

(b) Flap angle (β)

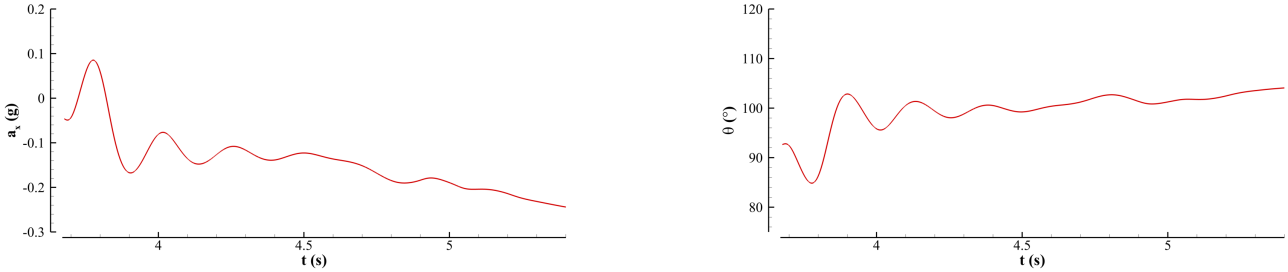

(c) Horizontal acceleration (a_x)

(d) Force vector angle (θ)

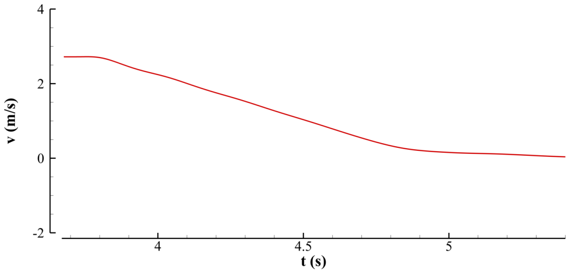

(e) Vertical speed (v)

Figure 16: Time history of key flight parameters during Phase II: (a) Propeller strength (ΔP), (b) Flap angle (β), (c) Horizontal acceleration (a_x), (d) Force vector angle (θ), and (e) Vertical speed (v).

5.3 Phase III: Horizontal acceleration

Phase III involves the horizontal acceleration of the 2D DS-CFJ airfoil. During this phase, the vertical speed is maintained at zero while the horizontal acceleration remains constant at 0.25 g. The airfoil accelerates horizontally to the desired cruise speed. As the horizontal speed increases, the flap angle (β) is gradually reduced to maintain a constant vertical force, which balances the total weight of the aircraft. Concurrently, the propeller strength (ΔP) decreases due to the increasing contribution of energy from the free stream as the horizontal speed rises. The force vector angle (θ) is maintained at 104.036° throughout this phase, ensuring the stability and effectiveness of the control strategy. Fig. 17 shows the Mach contours around the airfoil during this phase, from $t = 5.699\,\mathrm{s}$ to $t = 6.801\,\mathrm{s}$. It is observed that the flow remains attached to the airfoil, and the wake angle gradually changes to horizontal direction as the flap angle (β) continues to decrease, indicating effective aerodynamic control.

Downloaded by Gecheng Zha on August 16, 2024 | http://arc.aiaa.org | DOI: 10.2514/6.2024-4419

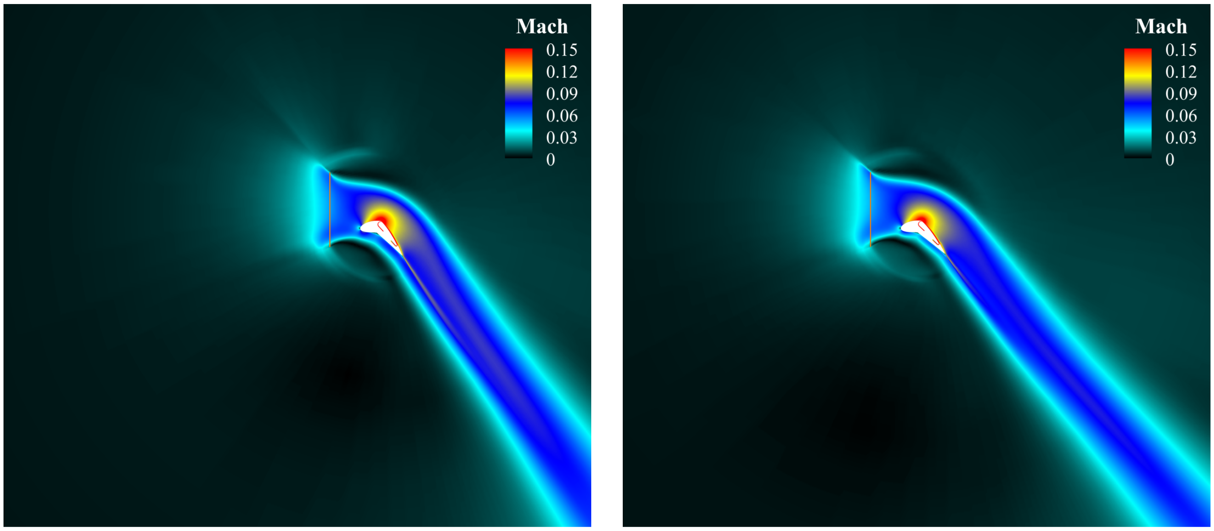

(a) $t = 5.699\,\mathrm{s}$ (b) $t = 6.066\,\mathrm{s}$

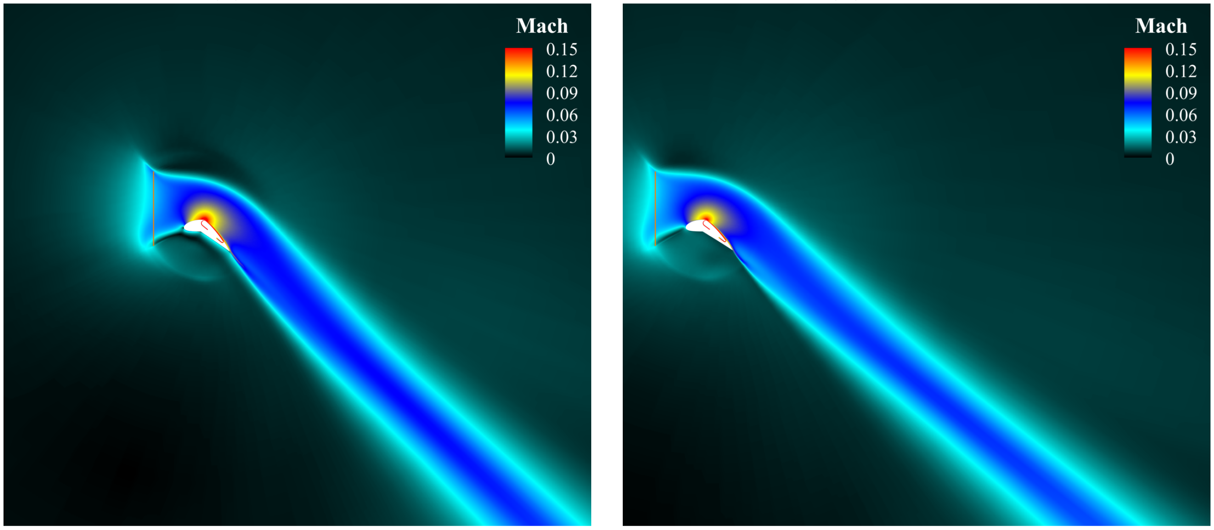

(c) $t = 6.434\,\mathrm{s}$ (d) $t = 6.801\,\mathrm{s}$

Figure 17: Mach contours around the DS-CFJ airfoil during Phase III at different time steps: (a) $t = 5.699\,\mathrm{s}$, (b) $t = 6.066\,\mathrm{s}$, (c) $t = 6.434\,\mathrm{s}$, (d) $t = 6.801\,\mathrm{s}$.

Fig. 18 presents the time history of key flight parameters during Phase III of the 2D DS-CFJ airfoil fluid-body interaction simulation. In Fig. 18(a), the propeller strength (ΔP) shows a gradual decrease as the horizontal speed increases, reflecting the reduced reliance on propeller thrust converting to lift due to the increasing contribution of dynamic pressure from the free stream. Fig. 18(b) illustrates the flap angle (β), which is about linearly decreasing to maintain a constant vertical force, balancing the aircraft's weight. Fig. 18(c) depicts the horizontal acceleration (a_x), which remains steady at 0.25 g, indicating consistent horizontal acceleration. Note the negative sign of the a_x is because the direction is opposite to the positive x-direction, not because it is decelerating. The vehicle is accelerating toward the cruise direction. Fig. 18(d) shows the force vector angle (θ), which is maintained at approximately 104.036°, ensuring stable aerodynamic control. Finally, Fig. 18(e) displays the vertical speed (v), which remains at zero throughout this phase, demonstrating effective control of vertical motion. These plots collectively demonstrate the effectiveness of the control strategies in achieving stable horizontal acceleration during Phase III.

Downloaded by Gecheng Zha on August 16, 2024 | http://arc.aiaa.org | DOI: 10.2514/6.2024-4419

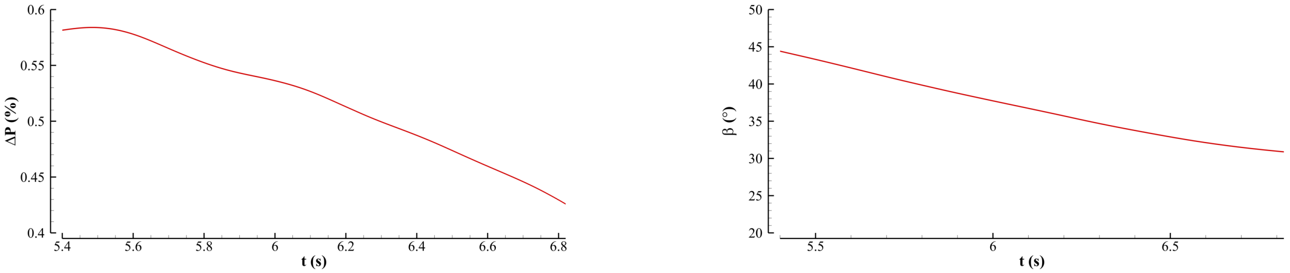

(a) Propeller strength (ΔP)

(b) Flap angle (β)

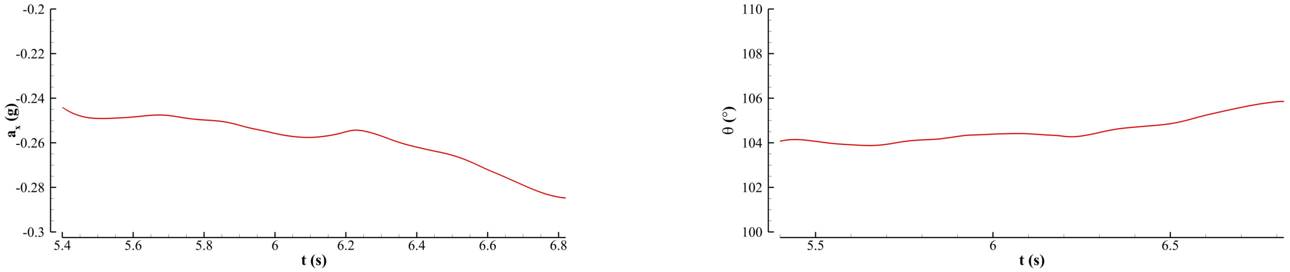

(c) Horizontal acceleration (a_x)

(d) Force vector angle (θ)

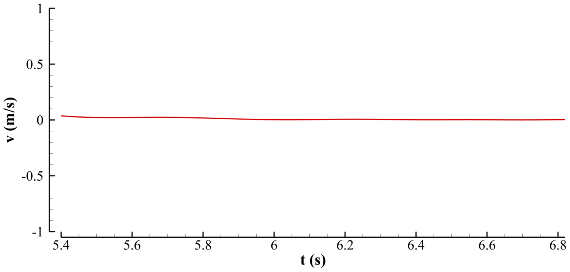

(e) Vertical speed (v)

Figure 18: Time history of key flight parameters during Phase III: (a) Propeller strength (ΔP), (b) Flap angle (β), (c) Horizontal acceleration (a_x), (d) Force vector angle (θ), and (e) Vertical speed (v).

6 Conclusions

The Fluid-Body Interaction hover-cruise transition for the DS-CFJ airfoil with a detailed examination of the transition flight, encompassing three distinct phases: Phase I: vertical takeoff; Phase II: transition; and Phase III: horizontal acceleration. The FBI procedure incorporates a high-fidelity structured grid CFD solver, automated mesh generation, and a 6-degree freedom body motion solver in a strongly coupled manner to accurately control and resolve the hover transition maneuver. In Phase I, the controlled vertical acceleration and subsequent steady vertical takeoff are successfully simulated, demonstrating stable control of vertical acceleration and resultant force angle. Phase II focuses on the transition phase, where vertical velocity is reduced to zero while achieving horizontal acceleration. The control algorithm effectively manages the flap angle β and propeller strength ΔP to maintain the desired force vector angle θ. Phase III involves horizontal acceleration to cruise speed, with consistent horizontal acceleration and maintaining zero vertical speed. The control algorithm shows high robustness in adapting to increasing horizontal speed by adjusting the flap angle and propeller strength to balance the aircraft's weight and maintain aerodynamic stability.

The results from these simulations highlight the effectiveness of the implicit coupling method in handling the dynamic fluid-body interactions during the transition flight of the DS-CFJ airfoil. A transient scaling law will be introduced to further understand and predict the unsteady transition dynamics. Detailed results and conclusions from these studies provide valuable guidelines for the future design and optimization of high-efficiency DS-CFJ aircraft.

7 Acknowledgment

This work is partially funded by NASA NIAC program with Grant Number 80NSSC24K0647. We greatly appreciate NASA's support.

Downloaded by Gecheng Zha on August 16, 2024 | http://arc.aiaa.org | DOI: 10.2514/6.2024-4419

References

[1] K. R. Antcliff, S. K. Whireside, L. W. Kohlman, and C. Silva, “Baseline Assumptions and Future Research Areas for Urban Air Mobility Vehicles.” AIAA Paper 2019-0528, AIAA SciTech 2019 Forum, San Diego, CA, 7-11 January 2019.

[2] National Academies of Sciences, Engineering, and Medicine , “Advanced Aerial Mobility: A National Blueprint (2020) .” Washington, DC: The National Academies Press, https://doi.org/10.17226/25646, 2020.

[3] T. Edwards and G. Price, “eVTOL Passenger Acceptance.” NASA Contractor Report 2020-220460, Jan. 2020.

[4] T. Edwards, “eVTOL Passenger Experience Final Report.” NASA Contractor Report HQ-E-DAA-TN70962, June 26, 2019.

[5] B. D. Adelstein, “Air Vehicle Factors Affecting Occupant Health, Comfort, and Productivity.” Vertical Flight Society 6th Annual Electric VTOL Symposium 2019, January 29-31, 2019.

[6] Yang, Y.-C. and Zha, G.-C., “Super-Lift Coefficient of Active Flow Control Airfoil: What Is the Limit?.” AIAA Paper 2017-1693, AIAA SCITECH2017, 55th AIAA Aerospace Science Meeting, Grapevine, Texas, 9-13 January 2017.

[7] R. E. Kuhn and J. W. Draper, “An Investigation of a Wing-Propeller configuration Employing Large-Chord Plain Flaps and Large-Diameter Propellers for Low-Speed Flight and Vertical Take-Off .” NACA TN-3307, December 1954.

[8] R. E. Kuhn and J. W. Draper, “Investigation of Effectiveness of Large-Chord Slotted Flaps in Deflecting Propeller Slipstreams Downward for Vertical Take-Off and Low-Speed Flight .” NACA TN-3364, Jan. 1955.

[9] R. E. Kuhn, “Investigation of the Effects of Ground Proximity and Propeller Position on the Effectiveness of a Wing with Large-Chord Slotted Flaps in Redirecting Propeller Slipstreams Downward for Vertical Take-Off .” NACA TN-3629, March 1956.

[10] Zha, G.-C. and Gao, W. and Paxton, C., “Jet Effects on Co-Flow Jet Airfoil Performance,” *AIAA Journal, No. 6,*, vol. 45, pp. 1222–1231, 2007.

[11] G.-C. Zha and D. C. Paxton, “A Novel Flow Control Method for Airfoil Performance Enhancement Using Co-Flow Jet.” *Applications of Circulation Control Technologies*, Chapter 10, p. 293-314, Vol. 214, Progress in Astronautics and Aeronautics, AIAA Book Series, Editors: Joslin, R. D. and Jones, G.S., 2006.

[12] Zha, G.-C and Paxton, C. and Conley, A. and Wells, A. and Carroll, B., “Effect of Injection Slot Size on High Performance Co-Flow Jet Airfoil,” *AIAA Journal of Aircraft*, vol. 43, 2006.

[13] Zha, G.-C and Carroll, B. and Paxton, C. and Conley, A. and Wells, A., “High Performance Airfoil with Co-Flow Jet Flow Control,” *AIAA Journal*, vol. 45, 2007.

[14] Wang, B.-Y. and Haddoukessouni, B. and Levy, J. and Zha, G.-C., “Numerical Investigations of Injection Slot Size Effect on the Performance of Co-Flow Jet Airfoil ,” *AIAA Journal of Aircraft*, vol. 45, pp. 2084–2091, 2008.

[15] B. P. E. Dano, D. Kirk, and G.-C. Zha, “Experimental Investigation of Jet Mixing Mechanism of Co- Flow Jet Airfoil.” AIAA-2010-4421, (5th AIAA Flow Control Conference, Chicago, IL), 28 Jun - 1 Jul 2010.

[16] B. P. E. Dano, G.-C. Zha, and M. Castillo, “Experimental Study of Co-Flow Jet Airfoil Performance Enhancement Using Micro Discreet Jets.” AIAA Paper 2011-0941, 49th AIAA Aerospace Sciences Meeting, Orlando, FL,, 4-7 January 2011.

[17] Lefebvre, A. and Dano, B. and Bartow, W. and Di Franzo, M. and Zha, G.-C., “Performance and Energy Expenditure of Co-Flow Jet Airfoil with Variation of Mach Number,” *AIAA Journal of Aircraft*, vol. 53, pp. 1757–1767, 2016.

[18] Lefebvre, A. and Zha, G.-C., “Numerical Simulation of Pitching Airfoil Performance Enhancement Using Co-Flow Jet Flow Control.” AIAA Paper 2013-2517, AIAA Applied Aerodynamics Conference, San Diego, CA, 24 - 27 June 2013.

[19] Lefebvre, A. and Zha, G.-C. , “Design of High Wing Loading Compact Electric Airplane Utilizing Co-Flow Jet Flow Control.” AIAA Paper 2015-0772, AIAA SciTech2015: 53rd Aerospace Sciences Meeting, Kissimmee, FL, 5-9 Jan 2015.

Downloaded by Gecheng Zha on August 16, 2024 | http://arc.aiaa.org | DOI: 10.2514/6.2024-4419

Downloaded by Gecheng Zha on August 16, 2024 | http://arc.aiaa.org | DOI: 10.2514/6.2024-4419

[20] Liu, Z.-X. and Zha, G.-C., “Transonic Airfoil Performance Enhancement Using Co-Flow Jet Active Flow Control.” AIAA Paper 2016-3472, AIAA AVIATION 2016, 8th AIAA Flow Control Conference, Washington, D.C, June 13-17, 2016.

[21] K.-W. Xu and G.-C. Zha, “High control authority 3d aircraft control surfaces using co-flow jet,” *AIAA Journal of Aircraft*, July 2020.

[22] G.-C. Zha, Y.-C. Yang, Y. Ren, and B. McBreen, “Super-lift and thrusting airfoil of coflow jet-actuated by micro-compressors.” AIAA Paper 2018-3061, AIAA AVIATION 2018, Atlanta, GA , 25 - 29 June 2018.

[23] Y. Wang and G.-C. Zha, “Study of 3D Co-flow Jet Wing Induced Drag and Power Consumption at Cruise Conditions.” AIAA Paper 2019-0034, AIAA SciTech 2019, San Diego, CA, January 7-11, 2019.

[24] Y. Wang, Y.-C. Yang, and G.-C. Zha, “Study of Super-Lift Coefficient of Co-Flow Jet Airfoil and Its Power Consumption.” AIAA Paper 2019-3652, AIAA Aviation 2019, AIAA Applied Aerodynamics Conference, Dallas, Texas, 17-21 June 2019.

[25] Yang, Y.-C. and Zha, G.-C., “Numerical Investigation of Performance Improvement of the Co-Flow Jet Electric Airplane.” AIAA Paper 2018-4208, AIAA AVIATION Forum 2018, 2018 Applied Aerodynamics Conference, Atlanta, Georgia, June 25-29, 2018.

[26] Y. Wang and G.-C. Zha, “Study of Mach Number Effect for 2D Co-Flow Jet Airfoil at Cruise Conditions.” AIAA Paper 2019-3169, AIAA Aviation 2019, AIAA Applied Aerodynamics Conference, Dallas, Texas, 17-21 June 2019.

[27] Y. Ren and G.-C. Zha, “Performance enhancement by tandem wings interaction of coflow jet aircraft.” AIAA Paper 2021-1823, 2021 AIAA SciTech Virtual Forum, 11-15 January, 2021.

[28] J. Boling, G.-C. Zha, and C. Zeune, “ Numerical Investigation of Coflow Jet Active Flow Control Swept Cylinders.” AIAA SciTech Forum 2020, Orlando, FL, 6-10 January, 2020.

[29] X. Chen and G.-C. Zha, “Implicit Application of Non-Reflective Boundary Conditions for Navier-Stokes Equations in Generalized Coordinates,” *International Journal for Numerical Methods in Fluids*, vol. 50, 2006.

[30] Shen, Y.-Q. and Zha, G.-C. and Chen, X.-Y., “ High Order Conservative Differencing for Viscous Terms and the Application to Vortex-Induced Vibration Flows,” *Journal of Computational Physics*, vol. 228(2), pp. 8283–8300, 2009.

[31] Y.-Q. Shen and G.-C. Zha, “Large Eddy Simulation Using a New Set of Sixth Order Schemes for Compressible Viscous Terms ,” *Journal of Computational Physics*, vol. 229, pp. 8296–8312, 2010.

[32] Shen, Y.-Q. and Zha, G.-C. and Wang, B.-Y., “ Improvement of Stability and Accuracy of Implicit WENO Scheme,” *AIAA Journal*, vol. 47, No. 2, pp. 331–344, 2009.

[33] Shen, Y.-Q. and Zha, G.-C. , “ Improvement of the WENO Scheme Smoothness Estimator,” *International Journal for Numerical Methods in Fluids*, vol. 64, p. DOI:10.1002/fld.2186, 2010.

[34] Shen, Y.-Q. and Zha, G.-C., “ Improved Seventh-Order WENO Scheme .” AIAA Paper 2010-1451, 48th AIAA Aerospace Sciences Meeting, Orlando, FL, Jan. 4-6, 2010.

[35] Y.-Q. Shen and G.-Z. Zha , “Generalized finite compact difference scheme for shock/complex flowfield interaction,” *Journal of Computational Physics*, vol. doi:10.1016/j.jcp.2011.01.039, 2011.

[36] Shen, Y.-Q. and Zha, G.-C., “ Low Diffusion E-CUSP Scheme with High Order WENO Scheme for Preconditioned Navier-Stokes Equations ,” *Journal of Computer and Fluids*, vol. doi:10.1016/j.compfluid.2011.10.013,, 2011.

[37] Y.-Q. Shen and G.-C. Zha, “Improvement of weighted essentially non-oscillatory schemes near discontinuities,” *Journal of Computer and Fluids*, vol. doi: http://dx.doi.org/10.1016/j.compfluid.2014.02.010, 2014.

[38] G.-C. Zha, Y. Shen, and B. Wang, “An improved low diffusion E-CUSP upwind scheme ,” *Journal of Computer & Fluids*, vol. 48, pp. 214–220, 2011.

[39] B.-Y. Wang and G.-C. Zha, “A General Sub-Domain Boundary Mapping Procedure For Structured Grid CFD Parallel Computation,” *AIAA Journal of Aerospace Computing, Information, and Communication*, vol. 5, No.11, pp. 2084–2091, 2008.

[40] Im, H.-S. and Zha, G.-C. and Dano, B. P. E., "Large Eddy Simulation of Coflow Jet Airfoil at High Angle of Attack," *Journal of Fluid Engineering*, vol. 136(2), p. 021101, 2014.

[41] Wang, B. Y and Zha, G.-C., "High Fidelity Simulation of Nonlinear Fluid-Structural Interaction with Transonic Airfoil Limit Cycle Oscillations," *Journal of Fluids and Structures*, vol. doi:10.1016/j.jfluidstructs.2010.02.003, 2010.

[42] K.-W. Xu and G.-C. Zha, "Mitigation of Serpentine Duct Flow Distortion Using CoFlow Jet Active Flow Control ." AIAA-2020-2954, AIAA Aviation 2020 Virtual Forum, 15-19 June, 2020.

[43] Y.-C. Yang, W. B. Bartow, G.-C. Zha, H.-Y. Xu, and J.-L. Wang, "Large eddy simulation of base drag reduction using jet boat tail passive flow control," *Journal of Computers and Fluids*, vol. 198, Feb. 2020.

[44] D. Espinal, H.-S. Im, and G.-C. Zha, "Full-annulus simulation of nonsynchronous blade vibration excitation of an axial compressor," *Journal of Turbomachinery*, vol. 140, pp. 031008–1, 2018.

[45] J.-Y. Gan, H.-S. Im, X.-C. Chen, G.-C. Zha, and C. L. Pasiliao, "Delayed detached eddy simulation of wing flutter boundary using high order schemes," *Journal of Fluids and Structures*, vol. 71, pp. 199–216, 2017.

[46] Im, H-S. and Zha, G-C., " Investigation of Flow Instability Mechanism Causing Compressor Rotor Blade Non-Synchronous Vibration ," *AIAA Journal*, vol. 52, pp. 2019–31, 2014.

[47] Im, H-S. and Zha, G-C., " Delayed Detached Eddy Simulation of Airfoil Stall Flows Using High Order Schemes ," *ASME Journal of Fluids Engineering*, p. DOI: 10.1115/1.4027813, 2014.

[48] X.-Y. Chen, G.-C. Zha, and M.-T. Yang, "Numerical Simulation of 3-D Wing Flutter with Fully Coupled Fluid-Structural Interaction," *Journal of Computers & Fluids*, vol. 36, No. 5, pp. 856–867, 2007.

[49] Gan, J.-Y. and Zha, G.-C., "Comparison of Drag Prediction Using RANS models and DDES for the DLR-F6 Configuration Using High Order Schemes." AIAA Paper 2016-0553, AIAA SCITECH2016, AIAA Aerospace Science Meeting, San Diego, CA, 4-8 January 2016.

[50] Wang, B. Y and Zha, G.-C., " Detached-Eddy Simulation of a Co-Flow Jet Airfoil at High Angle of Attack ," *AIAA Journal of Aircraft*, vol. 48, pp. 1495–1502, 2011.

[51] Im, H-S., Chen, X-Y and Zha, G-C., " Detached Eddy Simulation of Rotating Stall Inception for a Full Annulus Transonic Rotor ," *AIAA Journal of Propulsion and Power*, vol. 28, No. 4, pp. 782–798, 2012.

[52] K.-W. Xu, Y. Ren, and G.-C. Zha, "Separation control by coflow wall jet." Proceedings of AIAA Aviation 2021, Aug. 2-6, 2021, Submitted to AIAA Journal, 2-6 Aug. 2021.

[53] Y.-Q. Shen, G.-C. Zha, " A robust seventh-order WENO scheme and its applications." AIAA-2008-0757, 2008.

Downloaded by Gecheng Zha on August 16, 2024 | http://arc.aiaa.org | DOI: 10.2514/6.2024-4419